

# Solar irradiation regionalization in Uruguay: understanding the interannual variability and its relation to El Niño climatic phenomena

A. Laguarda<sup>a,\*</sup>, R. Alonso-Suárez<sup>a</sup>, R. Terra<sup>b</sup>

<sup>a</sup>*Laboratorio de Energía Solar, Instituto de Física, Facultad de Ingeniería, Universidad de la República, Montevideo, Uruguay.*

<sup>b</sup>*Instituto de Mecánica de los Fluidos e Ingeniería Ambiental, Facultad de Ingeniería, Universidad de la República, Montevideo, Uruguay.*

---

## Abstract

A regionalization of different characteristics of the solar resource is performed for Uruguay and surrounding areas (Southeastern South America). The input information consists of daily satellite estimates of Global Horizontal Irradiation (GHI) generated in a regular grid using a low uncertainty empirical satellite-based model which was specifically adapted for the region. Clusters are derived from the climatological annual cycle of monthly irradiation and clearness index and, separately, from time-series of monthly variability. The solar irradiation variability in each cluster is compared with El Niño South Oscillation (ENSO) signal. A high negative correlation is observed between ENSO and solar irradiance, most predominantly over February to May and November to December, particularly for the latter. This means that in a strong El Niño/La Niña year, solar irradiation values for the November-December period in Uruguay will be smaller/higher than the climatological

---

\*Corresponding author: A. Laguarda, laguarda@fing.edu.uy

average. These results are in agreement with the ones obtained for rainfall in other studies.

*Keywords:* Solar Radiation, Clustering, ENSO, k-means.

---

## 1 **1. Introduction**

2     The classification of an area into regions with similar climatic charac-  
3     teristics can guide the design of ground measurement networks suited for  
4     long-term renewable energy studies. The location of the measuring sites, if  
5     not adequate, may affect climatological studies related to the renewable ener-  
6     gies technology potential and long-term resource assessment. This is the case  
7     of solar irradiation and wind intensity, that highly vary in both space and  
8     time. These measurements, along with satellite images and/or atmospheric  
9     models, are the main tools to assess renewable energies resources. Associated  
10    uncertainties are directly translated to the financial risk of renewable energy  
11    projects. The regionalization also allows to better understand the impact of  
12    different large-scale climatic phenomena, such as the El Niño South Oscilla-  
13    tion (ENSO) on the regional renewable resource availability. These effects  
14    are better characterized over regions than over specific sites. This work fo-  
15    cuses on the monthly mean of global solar irradiation in a horizontal plane  
16    at ground level (GHI) and its monthly variability. The input information  
17    consists of daily satellite estimates of GHI obtained from a low uncertainty  
18    empirical satellite-based model, which was specifically adapted for the re-  
19    gional characteristics ([Alonso-Suárez et al., 2012, 2014](#)). The original hourly  
20    estimates, which are computed for this work for a 15 years time span on a  
21    regular grid of 31 points covering the region, are monthly averaged to analyze

its annual cycle and interannual variability. 22

Clustering techniques identify patterns in data without any a priori infor- 23  
mation, namely expert knowledge of predefined patterns. These techniques 24  
have been used for regionalization around the globe (Diabate et al., 2004; 25  
Zagouras et al., 2013, 2014, 2015; Polo et al., 2015; Watanabe et al., 2016). 26  
In Diabate et al. (2004) a set of hierarchical clustering methods are applied 27  
to annual cycles of clearness index's monthly averages at 62 sites in Africa 28  
to obtain different climatic zones across the continent. Other authors prefer 29  
to use non-hierarchical clustering techniques, such as the k-means method. 30  
Polo et al. (2015) use this methodology with daily sunshine hourly records 31  
to obtain a set of well-defined climatic regions for Vietnam. The cluster- 32  
ing is based on a variability index for each site that is calculated from the 33  
Cumulative Distribution Function (CDF) of daily solar irradiation obtained 34  
from the sunshine hours. Zagouras et al. (2014, 2015) also used the k-means 35  
algorithm, but applied to daily gridded irradiation records estimated with 36  
the satellite SUNY model (Perez et al., 2002). The clustering is applied af- 37  
ter reducing the dimensionality with Principal Component Analysis (PCA). 38  
The output was a set of regions for solar energy large-scale electricity ap- 39  
plications in the state of California. Zagouras et al. (2013) used the same 40  
algorithm with satellite cloud information for Greece to guide the design of 41  
a solar radiation monitoring network. Watanabe et al. (2016) classified 42  
47 ground measurement stations in Japan according to different metrics of so- 43  
lar radiation series for engineering applications. All these studies highlight 44  
the importance of identifying regions with similar solar variability, as it is 45  
associated with solar power fluctuations that can be a major challenge for 46

47 their grid integration. Clustering techniques have proven to be an efficient  
48 approach for regionalization purposes.

49 In this article we provide a first solar irradiation regionalization of Uruguay  
50 and surrounding areas. Different characteristics of solar irradiation are ana-  
51 lyzed, including resource monthly averages and anomalies. One of the goals  
52 of regionalization is to improve the description and understanding of the im-  
53 pact of large-scale climatic phenomena on the solar resource. In particular,  
54 the impact of the El Niño South Oscillation (ENSO) on this area is well  
55 known (Aceituno, 1988; Grimm et al., 2000), being the main climatic forcing  
56 in the region. Its impacts on local climate has been well established for some  
57 meteorological variables, in particular, on precipitation (Pisciottano et al.,  
58 1994) and streamflow (Mechoso and Pérez-Iribarren, 1992). However, the  
59 impact of ENSO on the regional solar irradiation has not been documented  
60 yet, and is a major contribution of this work.

61 This article is organized as follows. Section 2 and Section 3 describe the  
62 data and methodology, respectively. The results of the regionalization are  
63 presented in Section 4; Subsection 4.1 is based on the monthly annual cy-  
64 cles of mean irradiation and clearness index, while Subsection 4.2 focuses the  
65 variability of the monthly clearness index (monthly anomalies). Section 5  
66 describes the relationship between the ENSO and the clearness index vari-  
67 ability through correlation (Subsection 5.1), conditional stratification (Sub-  
68 section 5.2) and seasonal averages (Subsection 5.3). Finally, in Section 6 and  
69 Section 7, we present the final discussion and conclusions, respectively.

## 2. Data

70

The region under study is the country of Uruguay and close areas, a part of the broader Pampa Humeda region of the Southeastern part of South America. It is located between 30°S and 35°S (latitude) and 53°W and 58°W (longitude). The region is mainly rural and of low altitude, barely exceeding 500 meters in few places. Figure 1 illustrates the area location with a topography map for further reference.

76

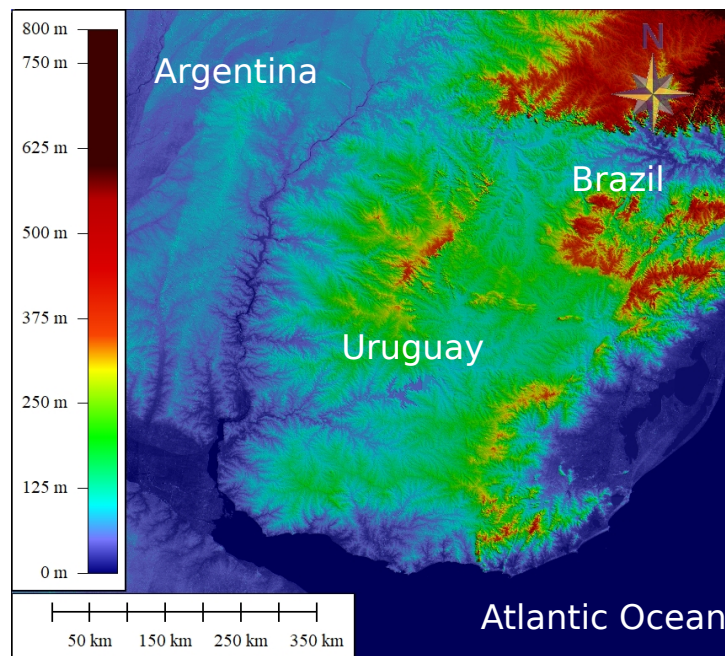


Figure 1: Topography map of the region with altitude data retrieved by the Terra-Aster NASA satellite information. Most of the area show heights under 500 m above the sea level.

The study requires long-term solar radiation data with adequate spatial coverage over the region. Solar radiation networks were first established in the country circa 2010, which implies that the ground measurements time

77

78

79

80 span is inadequate to define a climatology or appropriate to describe inter-  
81 annual variability. Further, ground measurements are not able to provide  
82 a high space resolution as the sites are located in sparse points in a larger  
83 territory. We, therefore, turn to solar irradiation estimates based on satel-  
84 lite imagery which can provide two decades data with a spatial resolution of  
85 few kilometers. [Subsection 2.1](#) describes the methodology to generate hourly  
86 and daily GHI estimates, while [Subsection 2.2](#) introduces the climate index  
87 associated to ENSO.

### 88 *2.1. Solar irradiation estimates*

89 Solar irradiation at the surface can be accurately estimated using models  
90 that use as input geostationary satellite images ([Perez et al., 2002](#); [Rigollier](#)  
91 [et al., 2004](#); [Ceballos et al., 2004](#); [Cebecauer et al., 2010](#); [Alonso-Suárez et al.,](#)  
92 [2012](#); [Qu et al., 2017](#); [Laguarda et al., 2020](#)). As the images are regularly  
93 available at a rate of more than two per hour and a nominal resolution  
94 of 1 km or less, they can be used as input to model a highly fluctuating  
95 phenomena like solar radiation. Satellite based models for snow free areas  
96 can use solely the visible channel images to quantify the cloudiness, which  
97 is the first factor affecting solar radiation availability at ground level. In  
98 colder sites, where snow might occur, the infrared images can be used to  
99 differentiate snow from clouds, as they both present a high albedo in the  
100 visible spectrum but differ in their temperature. More complex models ([Qu](#)  
101 [et al., 2017](#)) use multi-spectral satellite images to quantify cloud properties  
102 and then infer the ground solar irradiation. Satellite based models for solar  
103 irradiation assessment can be classified into physical ([Noia et al., 1993b](#))  
104 or empirical ([Noia et al., 1993a](#)), depending on their formulation. Physical

models attempt to model the radiative transfer thorough the atmosphere, so 105  
they require a detailed knowledge of the atmospheric state, including cloud 106  
type and cloud phase, water vapour content, aerosol optical depth, among 107  
others. The uncertainty of these models highly depend on the availability and 108  
quality of their input information. On the other hand, empirical models rely 109  
on simple statistical relationships between the ground solar irradiation and 110  
different variables that can be modelled, measured or calculated, including 111  
satellite information. These models are potentially accurate if high quality 112  
measurements are available in the target area to adjust their coefficients. 113  
The main disadvantage of statistical models is that the local adjustment can 114  
not be extrapolated globally. Some of the state-of-the-art models that are 115  
used worldwide for solar resource assessment do not fit perfectly in these two 116  
categories, like the SUNY model ([Perez et al., 2002](#)) or the former Heliosat 117  
versions ([Rigollier et al., 2004](#); [Beyer et al., 1996](#)), and they are referred as 118  
hybrid. These hybrid models have a physically-based formulation but some 119  
of their parameters are adjusted using ground measurements. 120

In this work we use an empirical satellite-based model that was specifi- 121  
cally adapted for the region to estimate ground level solar global irradiation 122  
at a horizontal plane ([Alonso-Suárez et al., 2012, 2014](#)). It uses GOES-East 123  
visible channel images of South America to estimate hourly irradiation via a 124  
statistical regression. This model was originally proposed by [Tarpley \(1979\)](#) 125  
and [Justus and Paris \(1986\)](#), and afterward was modified by [Alonso-Suárez](#) 126  
[et al. \(2012\)](#), resulting in a significant improvement on its performance. The 127  
model coefficients were adjusted using ground data from the Continuous Solar 128  
Irradiance Measurement Network (RMCIS) administrated by Universidad de 129

130 la República’s Solar Energy Laboratory (LES, <http://les.edu.uy>). The sta-  
131 tions of this network are located at semi-rural environments and record data  
132 at one minute intervals as the average of 15 seconds samples using spectrally  
133 flat Class A pyranometers (according to the ISO 9060:2018 standard). These  
134 pyranometers are calibrated every two years as recommended by the World  
135 Meteorological Organization (WMO). The calibration is done in accordance  
136 with the ISO 9847:1992 standard using a Secondary Standard pyranometer  
137 that the LES maintain with traceability to the World Radiometric Reference  
138 (WRR, World Radiation Center, Davos, Switzerland). This simple regres-  
139 sion model can provide hourly GHI estimates for the region with a negligible  
140 mean bias and a mean uncertainty of 14% (root mean square deviation ex-  
141 pressed as a percentage of the mean measurements value). Daily values are  
142 obtained from the accumulation of the intra-day hourly values. The daily  
143 estimates ( $H$ ) also show a negligible bias and have a reduced uncertainty  
144 of 7%. This performance is satisfactory when compared with commercial  
145 models commonly used in Europe and the USA, such as the Heliosat series  
146 (Rigollier et al., 2004; Qu et al., 2017) or the SUNY model (Perez et al.,  
147 2002). For this work we generate the satellite-derived daily irradiation data  
148 ( $H$ ) in a regular grid of  $1^\circ \times 1^\circ$  latitude-longitude distance (see Figure 2) for  
149 the period between January 2000 to December 2016 (17 years). In Figure 2  
150 the sites referred with 'U' lie within the Uruguayan territory, while A and B  
151 sites correspond to Argentina and Brazil respectively. The monthly averages  
152 ( $\overline{H}$ ) are obtained by averaging the daily values over each month. Months  
153 containing less than 15 valid days are discarded, leaving 189 out of the 204  
154 months of the period considered.



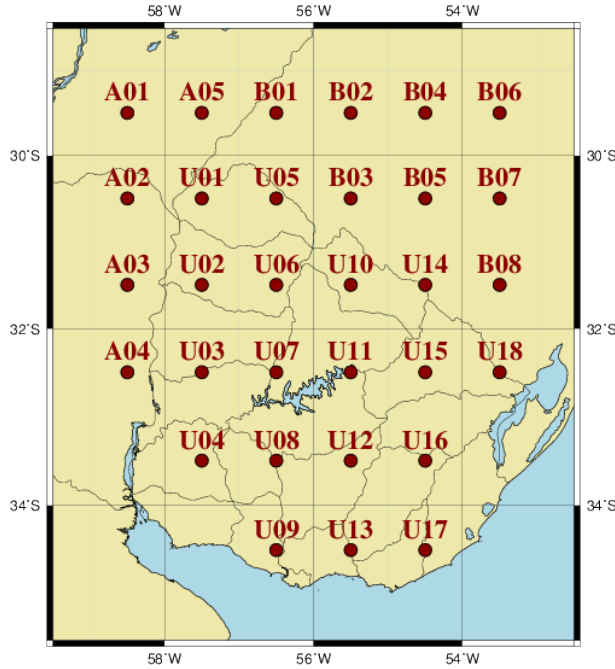


Figure 2: Locations used for generating monthly means of irradiation data (18 points in Uruguay, 8 points in Brazil and 5 in Argentina).

To remove the daily and seasonal geometrical behavior of the solar irradiation due to the sun's apparent movement, it is common practice to use the clearness index,  $K_t$ , which isolates the variability due to changes in the atmosphere (cloudiness, water content, aerosols, etc.) from the deterministic geometrical trend. This variable is defined at a monthly basis as,

$$K_t = \frac{\overline{H}}{\overline{H}_0} \quad (1)$$

where  $\overline{H}$  is the monthly average of the daily GHI measured values and  $\overline{H}_0$  is the monthly average of the daily irradiation on an horizontal plane at the top of the atmosphere,  $H_0$ . This daily variable can be calculated analytically for each site knowing the day of the year and latitude.

164 *2.2. El Niño*

165 There are several indices to quantify ENSO phenomenon. However, the  
166 most widely used index in research, monitoring and reporting is the Niño 3.4  
167 index (N3.4) which represents the average sea surface temperature anomaly  
168 over a region in the central equatorial Pacific Ocean, between 5°N–5°S and  
169 170°W–120°W (Trenberth, 1997). The N3.4 information is publicly avail-  
170 able at [www.cpc.ncep.noaa.gov](http://www.cpc.ncep.noaa.gov), from where we retrieved the data. Each  
171 monthly value corresponds to the average of the trimester centered in the  
172 corresponding month.

173 **3. Methodology**

174 In this work three solar radiation regionalizations are obtained through  
175 well known clustering techniques, based on yearly cycles of  $\bar{H}$  and  $K_t$ , and on  
176  $K_t$  monthly anomaly time series. Using the latter, the interannual variability  
177 of the solar resource and its seasonal varying association with ENSO climatic  
178 phenomena is studied in detail.

179 *3.1. Regionalization*

180 A first set of two regionalizations is performed over the annual cycles of  
181  $K_t$  and  $\bar{H}$ , i.e. 12 dimensions vectors, one for each of the 31 sites showed  
182 in [Figure 2](#). We start with all the 31 sites and use the Ward hierarchical  
183 agglomerative algorithm (Wilks, 2011) to sequentially group the individuals,  
184 minimizing intra-group variance based on the Euclidian distance on the 12-  
185 dimensional space, up to a final number of clusters set to three. The centroids  
186 of these clusters constitute the seeds of the non-hierarchical k-means methods

that regroups all individuals to the nearest centroid (using the same distance 187  
as before), recalculates the centroids and proceeds iteratively until individuals 188  
no longer change of cluster. The combined algorithms do not include any a 189  
priori information, such as seeds, being the final number of clusters the only 190  
subjective parameter, which will prove a reasonable choice in view of results 191  
in [Section 4](#). Further details of both clustering methods can be found in 192  
[Duda et al. \(2001\)](#); [Wilks \(2011\)](#). 193

Next, a different regionalization is made using the  $K_t$  interannual anomaly 194  
time series as the attribute at each site. First, we perform a principal compo- 195  
nent analysis (PCA) of the initial data to reduce the dimensionality without 196  
losing significant information. The initial data here is a set of 31 vectors - 197  
one per grid point- of 202 monthly anomaly values of  $K_t$ . The PCA converts 198  
an initial set of correlated variables into a sequence of uncorrelated linear 199  
combinations of said variables, the principal components, each contributing 200  
a decreasing portion of the total variance. It is, then, possible to rank the 201  
principal components and select a reduced set that explains most of the vari- 202  
ance of the original data set. More details of the method can be found in 203  
[Jolliffe \(2002\)](#); [Bishop \(2006\)](#). As it is shown in [Subsection 4.2](#), five princi- 204  
pal components are retained, which explain most of the associated variance. 205  
Then, the same combined Ward plus k-means methodology is used with the 206  
only difference that the distance  $d$  selected in this case, for both clustering 207  
methods, is based on Pearson correlation instead of the Euclidean distance: 208

$$d(\mathbf{x}_i, \mathbf{x}_j) = 1 - \text{corr}(\mathbf{x}_i, \mathbf{x}_j), \quad (2)$$

where  $\mathbf{x}_i$  and  $\mathbf{x}_j$  are monthly  $K_t$  anomaly series. This distance is appropriate 209

210 in this case because we aim to find clusters whose mean solar irradiation is  
211 well correlated with ENSO.

### 212 *3.2. Impact of ENSO in the regional solar radiation*

213 The second part of this work focuses on the study of the influence of  
214 ENSO on the monthly anomalies of  $K_t$  behavior. The work considers several  
215 stages, from exploratory to deeper analysis. Firstly, the Pearson correlation  
216 is computed between each cluster's monthly  $K_t$  anomalies and the N3.4 in-  
217 dex time-series. Each cluster's centroid is considered as it represents the  
218 average value within the cluster. An exploration of how these  $K_t$  anomalies  
219 stratify with the N3.4 index is also done. For stratification, two situations  
220 on N3.4 index are distinguished: greater than  $+0.5$  °C (named positive) or  
221 less than  $-0.5$  °C (named negative). By using the Wilcoxon-Mann-Whitney  
222 (WMW) classical non parametrical test, stratified according to the sign of  
223 simultaneous N3.4 values, we tested if the two stratified data sets came or  
224 not from the same probability distribution. Unfortunately, this test hypoth-  
225 esis could not be rejected in this work to a 95% confidence level using the  
226 monthly data time-series. Instead, we grouped the data considering that  
227 the influence of ENSO on the region ranges from October to next year July  
228 (Pisciottano et al., 1994), so we use the N3.4 index averaged during the peak  
229 season of extreme events (November to January, N3.4-NDJ) to stratify the  
230 monthly  $K_t$  anomalies from the preceding September to the following Au-  
231 gust. In other words, we tag a complete year (from September to August)  
232 according to N3.4-NDJ's sign only, and then we apply the WMW test for  
233 each cluster. This is applied to the yearly monthly time-series and does not  
234 provide information of the seasonality of the effect.

To obtain more information from the stratification, in particular regarding 235  
seasonality, the test is applied also to stratified data sets for each month 236  
and for each cluster separately. In order to have enough data, the test is 237  
performed over twelve 3-months moving-window periods. For instance, for 238  
March, the test is performed with data corresponding to February, March 239  
and April stratified with  $N3.4-NDJ > +0.5 \text{ }^\circ\text{C}$  and  $N3.4-NDJ < -0.5 \text{ }^\circ\text{C}$ . 240  
Using this procedure, we identify seasons in which the stratified behavior of 241  
 $K_t$  anomalies are categorically different. After identifying the season with 242  
noticeable ENSO effect, the correlation is also computed for the periods 243  
identified. To correlate these seasonal  $K_t$  anomalies with N3.4-NDJ index, 244  
the  $K_t$  anomalies are averaged over each season and year, and Pearson's 245  
correlation is computed between each clusters seasonal averages and N3.4- 246  
NDJ. Finally, this calculation is repeated for the same identified periods, but 247  
for each of the 31 sites individually, without considering the clusters. This 248  
allow us to obtain a correlation map in where the spatial distribution of the 249  
ENSO effect can be seen. 250

#### 4. Clustering results 251

Clustering results are shown in this section, first applied to the annual 252  
cycles of  $\bar{H}$  and  $K_t$  and then to the time series of monthly anomalies of  $K_t$ . 253

##### 4.1. Clustering by climatological annual cycles 254

To distinguish regions according to the mean solar irradiation, the annual 255  
cycle of  $\bar{H}$  is used as input for the k-means/Ward algorithm. [Figure 3](#) shows 256  
the clustering result when the irradiation values are used. The procedure 257  
is repeated using the monthly average of the  $K_t$ , to exclude the geometrical 258

259 effect of latitude and the resulting clusters are shown in [Figure 4](#). As can  
260 be seen in [Figure 3](#), solar resource increases mainly from South to North  
261 (closer to Equator) with a slight east/west gradient, resulting in a south-east  
262 to north-west increasing trend. This result is in accordance with local so-  
263 lar maps ([Abal et al., 2010](#); [Alonso-Suárez et al., 2014](#)). The arrangement  
264 of the clusters in [Figure 4](#) (due mainly to cloudiness) has a stronger tilt in  
265 the spatial trend than in the case of the irradiation clustering, more aligned  
266 with the North-South line. Lowest  $K_t$  values are observed along the Atlantic  
267 Ocean coast (coast eastern to  $55^\circ\text{W}$  longitude) while highest  $K_t$  values are  
268 observed North-West inland. Both spatial clustering provide an interesting  
269 interpretation of the solar resource space distribution in the region: the irra-  
270 diation trend is a result of combining a cloudiness trend ( $K_t$ ), more aligned to  
271 increase for West to East and more affected by the Atlantic Ocean proximity,  
272 with the latitude effect, that is associated with a South to North increasing  
273 trend of the extraterrestrial irradiation ( $H_o$ ).

274 [Figures 5](#) and [6](#) show, respectively for irradiation and  $K_t$ , the annual  
275 cycle for the entire domain (left) and the anomalous annual cycle for each  
276 cluster's centroid (right). Irradiation annual cycle over the entire region has  
277 a minimum peak in June-July and a maximum peak in December-January,  
278 as expected.  $K_t$  annual cycle shows that, compared to the annual average,  
279 slightly more clouds are observed in local winter (June) and slightly more  
280 clear skies are observed in local summer (December-January). The center  
281 cluster has a similar behavior to the entire domain in both cases. The other  
282 two clusters exhibit an above and below trend in relation with the average.  
283 Irradiation largest anomalies are observed during intermediate seasons, and

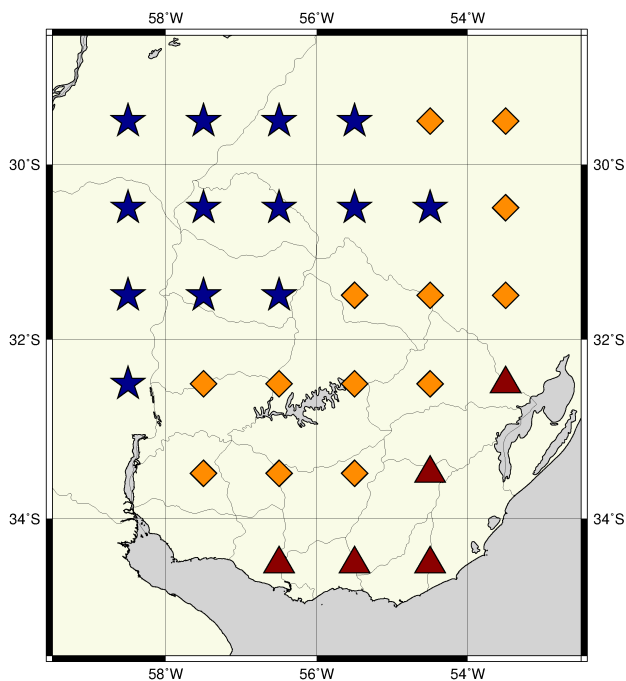


Figure 3: The three clusters found (see shapes and/or colors) according to annual cycles of monthly irradiation.

in August in particular. Cloudiness largest anomalies are observed also during August-September, but also December-January. The minimum difference between clusters is observed in local winter (June).

#### 4.2. Clustering by seasonal and interannual variability

To identify regions with coherent seasonal and interannual variability of the solar resource, the monthly anomalies of  $K_t$  in the period 2000-2016 are used as the grid-point attributes. To simplify the time-series (31 vectors -one per grid point- of 202 monthly anomaly values of  $K_t$ ), leaving only the more dominants effects, a PCA is applied. PCA returns a smaller dimensional subspace of the data that retains most of the original data information, reducing

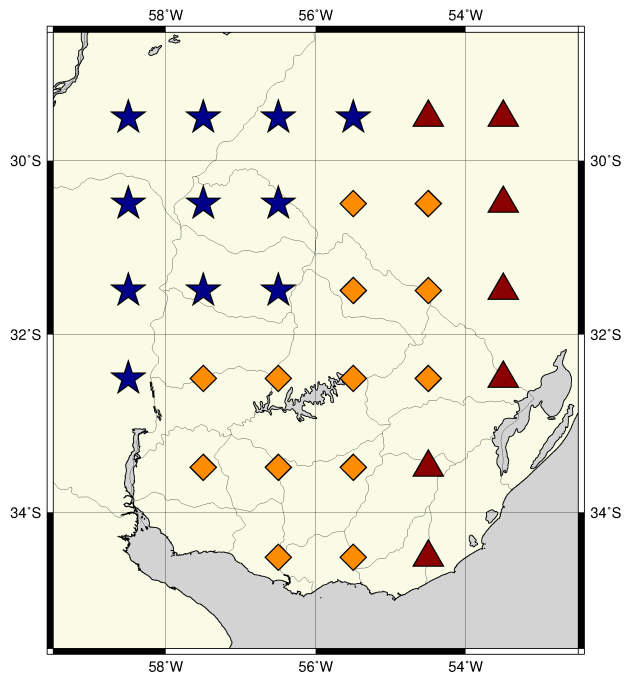


Figure 4: The three clusters found (see shapes and/or colors) according to annual cycles of monthly clearness index.

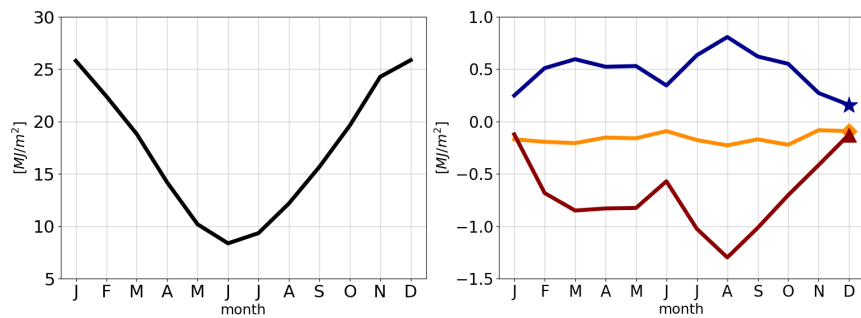


Figure 5: Mean annual cycle of monthly irradiation over the entire domain (left). Anomalous annual cycle for each cluster centroid (right). The triangle, diamond and star shapes correspond to Fig. 3.



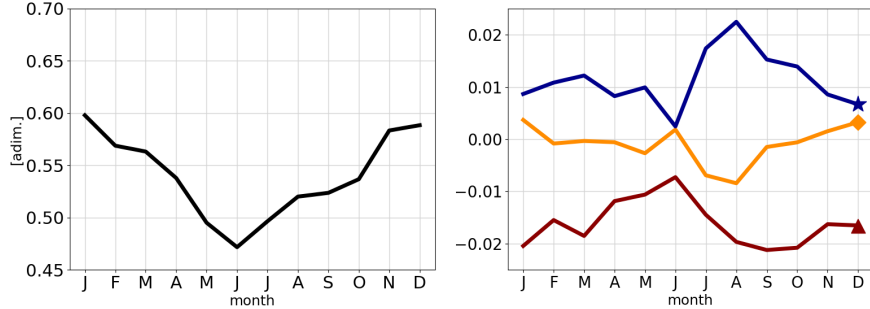


Figure 6: Mean annual cycle of monthly clearness index over the entire domain (left). Anomalous annual cycle for each cluster centroid (right). The triangle, diamond and star shapes correspond to Fig. 4

the complexity of the signal and filtering non typical effects. In this case, 294  
the first five principal components represent 92.6% of the total variance, so 295  
the clustering analysis is performed in the reconstructed time series based on 296  
these 5 main modes. The clusters obtained (see Figure 7) show a dominant 297  
latitudinal arrangement with a tilt perpendicular to the coast, contrary to 298  
the clusters performed based on the irradiation annual cycle. 299

Considering that ENSO is the main source of interannual variability in 300  
the region and its effects are known to vary both spatially and seasonally 301  
(Aceituno, 1988; Cazes-Boezio et al., 2003), these clusters will be used in 302  
the next section to quantify the ENSO effect. The rationale behind this 303  
is that these clusters represent better the interannual variability of solar 304  
irradiation in the region. These clusters were derived by using the correlation 305  
as distance (Eq. (2)), thus they are better suited for the correlation analysis 306  
in the following section. 307

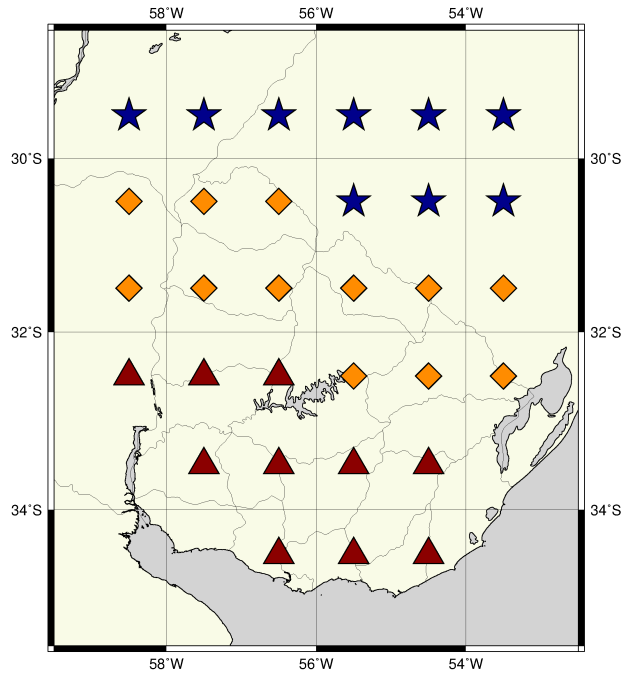


Figure 7: The three clusters found (see shapes and/or colors) according to monthly clearness index anomaly time series.

## 308 5. Influence of ENSO

309 In this section we explore the interannual variability of the solar resource  
 310 and its seasonal variations in association with ENSO climatic phenomena.  
 311 For this analysis the  $K_t$  anomalies are used, filtering the seasonal cycle and  
 312 climatological trend, and isolating the results from the seasonal influence.

### 313 5.1. Correlation

314 [Table 1](#) shows the Pearson correlation between the monthly N3.4 Index  
 315 and the clearness index anomaly for each cluster average ([Figure 7](#)), together  
 316 with p-value of the Student test. As mentioned in [Section 3](#), correlations  
 317 computed in this way do not account for the seasonality of ENSO signal

in the local climate, which is known to be significant (Cazes-Boezio et al., 2003). The values obtained are still negative in all cases, although rather small. Note that high N3.4 signal is associated with wetter and cloudier weather in the region, therefore with lower clearness indices. Notably, the northern cluster, where a strongest ENSO signal is expected (Pisciottano et al., 1994), shows a correlation that is significant to a 99% confidence level ( $1 - p \approx 99\%$ ), which is a very high value.

	Correlation	p-value
Southern Cluster (triangles)	-0.105	0.1386
Central Cluster (diamonds)	-0.137	0.0512
Northern Cluster (stars)	-0.183	<b>0.0091</b>

Table 1: Correlation between the cluster’s centroids in terms of  $K_t$  anomaly and the N3.4 index. The third column indicates the p-value of the t-Student test.

## 5.2. Stratification

In this subsection, we explore how the clearness index stratifies with ENSO. As mentioned in Section 3, the WMW test results are not clear to quantify if data, stratified according to simultaneous N3.4 ( $> +0.5$  °C and  $< -0.5$  °C), come from the same statistical distribution or not. According to the local period of influence of N3.4 signal (Pisciottano et al., 1994), the test is performed over the sets of data stratified according to N3.4-NDJ for each cluster. In this scenario, the test rejects the null hypothesis with a confidence of 95% for all the clusters. This means that the data behaves differently according to the sign of N3.4-NDJ (p-values of 0.0021 for star-shaped sites in

335 Figure 7, 0.0029 for diamond-shaped and 0.0426 for triangle-shaped). Figure  
 336 8 shows the empirical Cumulative Distribution Functions (CDF) of  $K_t$   
 337 anomaly for each cluster for all data discriminated according to N3.4-NDJ  
 338  $> +0.5$  °C (red) and N3.4-NDJ  $< -0.5$  °C (blue), jointly with the all data  
 339 CDF (black). The WMW test for each month separately was repeated and  
 340 the three clusters showed different distributions (i.e. discard null hypothesis)  
 341 mainly for March, April, November and December. In Table 2 the p-Values  
 342 of the test performed over each month over the clusters are shown. We fur-  
 343 ther analyze the influence of N3.4-NDJ within the year. Figure 9 showing  
 344 the annual cycles of  $K_t$  anomaly conditioned to N3.4-NDJ.

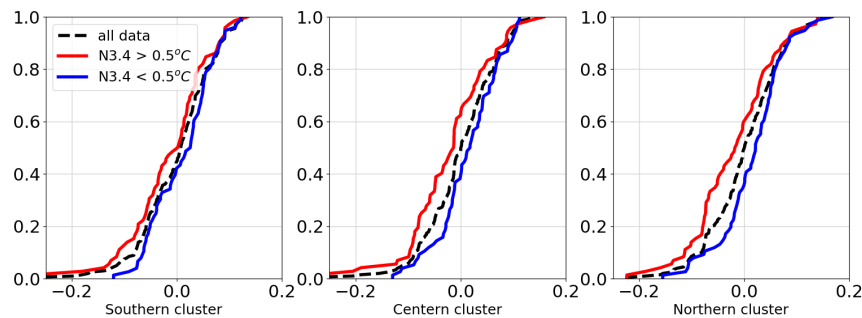


Figure 8: Empirical Cumulative Distribution Function (ECDF) of the monthly  $K_t$  anomaly for each cluster discriminating according to ENSO-NDJ. The black dashed line denotes the ECDF without ENSO discrimination.

### 345 5.3. Seasonability

346 In light of the previous subsection's results, we further analyze the in-  
 347 fluence of ENSO signal on the  $K_t$  anomaly for specific seasons: November-  
 348 December and February to May, which largely coincide with the main seasons

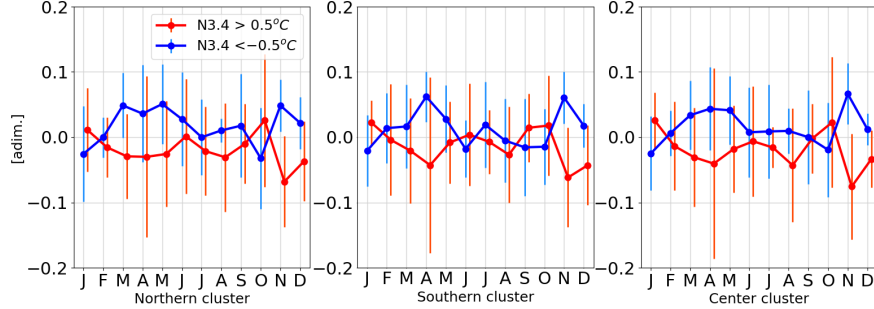


Figure 9: Each chart shows the annual cycles of  $K_t$  anomaly for each cluster discriminating according to N3.4-NDJ. The x-axis corresponds to the month. The dots represent the mean value for each month, while the bars represent the standard deviation.

of influence of ENSO on the local climate (Pisciottano et al., 1994). In or- 349  
 order to correlate the  $K_t$  anomalies with N3.4-NDJ index, the  $K_t$  anomalies 350  
 are averaged over each season. The p-values for these seasons are shown in 351  
 Table 3, which shows that the  $K_t$  anomaly stratified according to the sign of 352  
 N3.4-NDJ belong to different probability distribution with a high confidence 353  
 level ( $1 - p \geq 99\%$ ) for November-December season, but not for February 354  
 to May. Results, which capture the interannual variability of the seasonally 355  
 averaged influence of ENSO on the clearness index, are shown in Table 4. 356

Lastly, we analyze the spatial variability of ENSO influence on  $K_t$  anoma- 357  
 lies for these selected seasons independently of the clusters. A correlation 358  
 map between anomaly  $K_t$  series over the Nov-Dec and Feb-May periods with 359  
 the N3.4-NDJ index is performed and results are shown in Figure 10. For the 360  
 case of the Nov-Dec season, all sites are correlated with a 95% of confidence. 361  
 The same holds for the Feb-May case with the exception of the three coastal 362  
 points. Figure 11 shows the scatter plot of the clearness index, spatially 363

	Northern cluster (star)	Center cluster (diamond)	Southern cluster (triangle)
Jan	0.339	0.773	0.554
Feb	0.335	0.693	0.987
Mar	<b>0.026</b>	<b>0.035</b>	<b>0.064</b>
Apr	<b>0.006</b>	<b>0.012</b>	<b>0.030</b>
May	0.056	0.056	0.169
Jun	0.103	0.117	0.537
Jul	0.235	0.179	0.837
Aug	0.176	0.133	0.939
Set	0.988	0.826	0.511
Oct	0.266	0.231	0.455
Nov	0.088	<b>0.041</b>	<b>0.020</b>
Dec	<b>0.017</b>	<b>0.042</b>	<b>0.022</b>

Table 2: p-values of the WMW test for twelve trimesters discriminated according to N3.4-NDJ  $> 0.5^{\circ}C$  and N3.4-NDJ  $< -0.5^{\circ}C$  for each cluster.

	November-December series	February to May series
Southern cluster (triangle)	<b>0.0006</b>	0.8235
Center cluster (diamond)	<b>0.0008</b>	0.5034
Northern cluster (star)	<b>0.0009</b>	0.1388

Table 3: p-values of the WMW test for November-December and February to May of clearness index anomaly discriminated according to ENSO  $> +0.5^{\circ}C$  and ENSO  $< -0.5^{\circ}C$  for each cluster.

	November-December		February to May	
	correlation	p-value	correlation	p-value
Southern cluster (triangles)	-0.704	<b>0.0016</b>	-0.519	<b>0.0395</b>
Central cluster (diamonds)	-0.852	<b>&lt;0.0001</b>	-0.586	<b>0.0170</b>
Northern cluster (stars)	-0.868	<b>&lt;0.0001</b>	-0.594	<b>0.0152</b>

Table 4: Correlation and p-value for between N3.4-NDJ and seasonally averaged clearness index for each cluster. All correlations are statistically significant at 95% of confidence.

averaged over all sites that exhibit significant correlations (those depicted 364  
in [Figure 10](#)), and the N3.4-NDJ index, evidencing the strong influence of 365  
ENSO on the interannual variability of the solar resource in the selected sea- 366  
sons. To emphasize this behavior, the linear regression is added to the plot 367  
in order to visualize the trend. 368

## 6. Discussion 369

We characterized the spatio-temporal variability of the solar resource over 370  
a region of Southeastern South America -containing Uruguay- based on 17- 371  
years-long monthly series of solar irradiation. The 31-points gridded data 372  
set was derived from hourly estimates based on satellite imagery with a spa- 373  
tial resolution of few kilometers, validated against high accuracy radiometric 374  
land stations. A cluster analysis was performed based on the mean annual 375  
cycle (12 monthly values) of both solar irradiation and clearness index, ren- 376  
dering three regions in each case. Solar irradiation grows from southeast 377  
to northwest, consistent with existent solar maps, showing minimum spatial 378

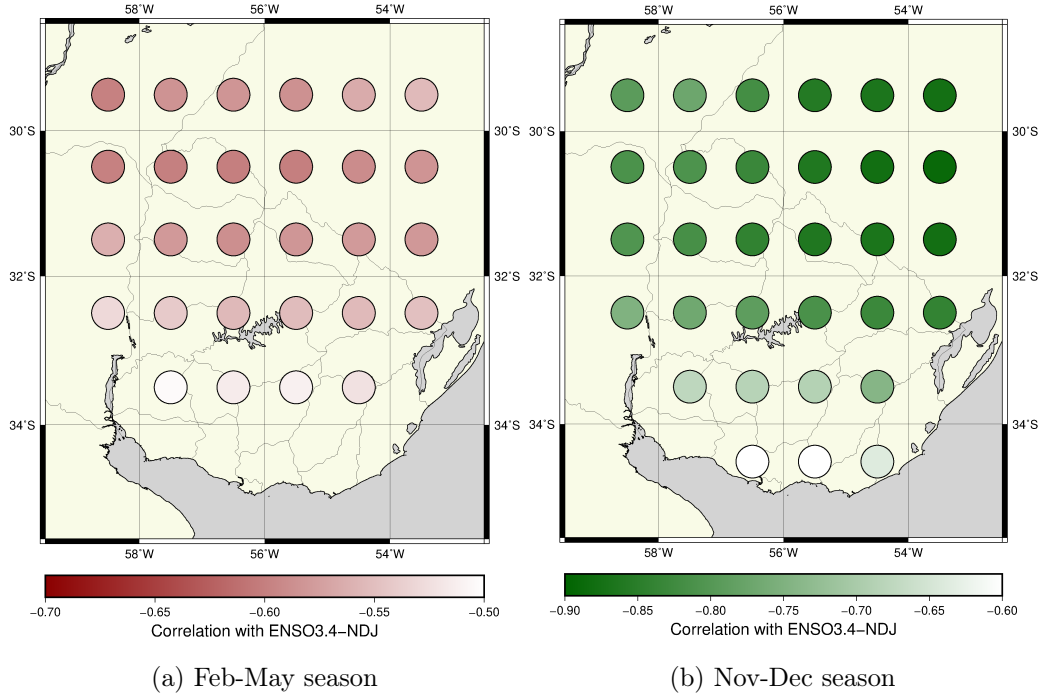


Figure 10: Correlation map between each site and the N3.4-NDJ for February-May (left) and November-December (right) seasons. Only sites with correlations significant to a 95% confidence level are shown.

379 differences between clusters during -austral- summer. This is due to the lat-  
 380 itudinal variation of daily irradiation at the top of the atmosphere combined  
 381 with the spatial distribution of the clearness index ( $K_t$ ). The latter shows  
 382 clusters that arrange roughly from east to west, with  $K_t$  increasing inland  
 383 throughout the year, a reflection of the larger humidity and cloudiness closer  
 384 to the Atlantic coastline. Largest differences between clusters occur from late  
 385 winter through early fall, when the clearness index in the most continental  
 386 cluster is approximately between 6% and 9% greater than that of the more coastal  
 387 region.



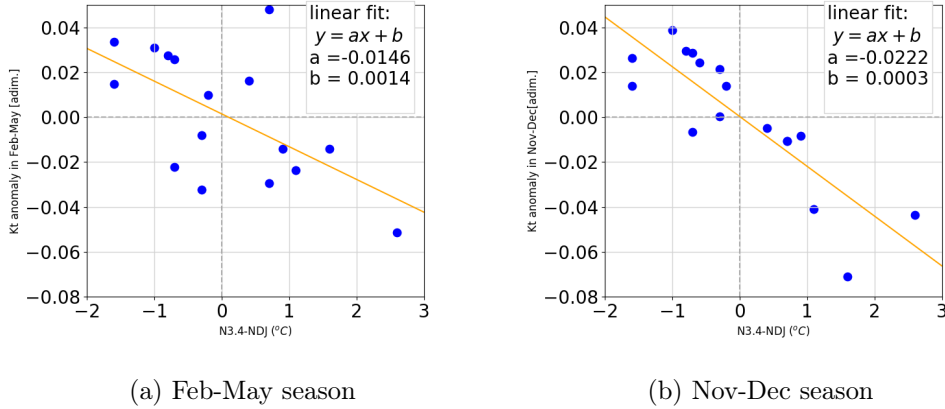


Figure 11: Linear regression of spatial average of the  $K_t$  February-May (left) and November-December (right) anomaly of the sites with a 95% confidence correlation with N3.4-NDJ. The linear regression added to the plot is not intended to model the behavior of the  $K_t$  anomaly but to illustrate its trend.

Next, we focused on interannual variability, which may be of interest for 388  
the management of an interconnected electric system with a large partici- 389  
pation of solar energy. A cluster analysis was again performed, this time 390  
using the entire  $K_t$  anomalies time series as the attribute for each grid point 391  
and a correlation-based distance. The resulting clusters arrange from south- 392  
southwest to north northeast, with a different orientation of those based on 393  
the climatological annual cycle. Only the time series of the northernmost 394  
cluster shows marginally significant anti-correlation with ENSO, the largest 395  
source of interannual variability in the region. However, it is well known that 396  
ENSO signal on the regional climate is seasonal dependent, a property that is 397  
not captured in this cluster analysis. Therefore, an ENSO based stratification 398  
of the clearness index time series associated with each cluster was performed 399

400 on moving trimesters. The results confirm previous studies of ENSO influ-  
401 ence on the local climate (mainly on precipitation) that have identified late  
402 spring and early summer as the main season of influence and fall as a second  
403 -less significant- one. For November-December (February-May), the correla-  
404 tion of N3.4-NDJ with the centroid of every cluster is statistically significant  
405 to a 99% (95%) level, with increasing correlation to the north.

406 Motivated by the previous results, correlation between N3.4-NDJ and sea-  
407 sonal mean  $K_t$  for every grid point were computed for each season (November-  
408 December and February-May). The resulting correlation maps and associ-  
409 ated scatter plots quite clearly show the strength and spatial distribution of  
410 ENSO signal in those seasons. This is consistent with previous studies for  
411 other variables, although the strength of the correlation during February-May  
412 seems higher than what has been reported for precipitation.

## 413 7. Conclusion

414 A first comprehensive regionalization of Uruguay’s solar resource was per-  
415 formed with three different attributes of this variable, in all cases obtaining  
416 three spatial clusters. In the first case, based on GHI mean annual cycle, the  
417 results show the expected Southeast to Northwest gradient in total irradiation,  
418 consistent with previous solar resource climatological maps ([Abal et al., 2010](#);  
419 [Alonso-Suárez et al., 2014](#)). In the second case, based on the clearness  
420 index mean annual cycle, the arrangement of the clusters shows an increase  
421 in  $K_t$  from East to West, associated with decreasing cloudiness inland. The  
422 third case, based on the interannual variability of the clearness index, results  
423 in clusters arranged from the Southwest to the Northeast. This last region-

alization depicts clusters with similar clearness index anomalies (indicating 424  
temporal variability) at the monthly time-scale and can thus contribute to 425  
the management of the solar resource in the region. It is well established that 426  
ENSO has a significant seasonal impact on the climate of the region during 427  
extreme phases of this cuasi-periodic oscillation of the climate system, known 428  
as El Niño and La Niña. ENSO signal in the local hydro-climate is of such 429  
relevance, that the associated N3.4 index is already included in the electric 430  
system simulator used for planning and dispatch (Maciel et al., 2015), in 431  
particular due to its impact in the hydroelectric component of the system. It 432  
is thus natural to explore the relation between the solar resources and N3.4 433  
index. In this sense, the most important result is the determination of a high 434  
negative correlation between ENSO (as represented by N3.4 index) and solar 435  
irradiation variations (as represented by  $K_t$  anomalies). This anti-correlation 436  
is more significant over the February-May and November-December periods, 437  
and allows to conclude with high confidence level ( $\geq 99\%$  for the former pe- 438  
riod and  $\geq 96\%$  for the latter) that during El Niño years lower solar resource 439  
will be available in the region, specially over the center and Northern region. 440  
The opposite occurs during La Niña years. 441

These results are very promising and potentially useful for the design of 442  
solar irradiation measurements networks and for the management of inte- 443  
grated electrical systems with increasing contributions of solar energy. A 444  
second stage of this study, in order to obtain further and more detailed infor- 445  
mation, would be to reassess the results with longer time series and higher 446  
resolution grids, which may allow to include sub-seasonal variability in the 447  
ENSO analysis. 448

## 449 Acknowledgments

450 The authors thank Mr. Martin Benenati that kindly provided the topog-  
451 raphy map of [Figure 1](#) based on the Terra-Aster NASA satellite data.

## 452 References

453 Abal, G., D'Angelo, M., Cataldo, J., and Gutiérrez, A. (2010). *Mapa Solar*  
454 *del Uruguay, versión 1.0*. UCUR, Montevideo, Uruguay.

455 Aceituno, P. (1988). On the functioning of the southern oscillation in the  
456 south american sector. part 1: surface climate. *Monthly Weather Review*,  
457 116:505–524.

458 Alonso-Suárez, R., Abal, G., Musé, P., and Siri, R. (2014). Satellite-derived  
459 solar irradiation map for Uruguay. In *Elsevier Energy Procedia*, volume 57,  
460 pages 1237–1246.

461 Alonso-Suárez, R., Abal, G., Siri, R., and Musé, P. (2012). Brightness-  
462 dependent Tarpley model for global solar radiation estimation using GOES  
463 satellite images: application to Uruguay. *Solar Energy*, 86(11):3205–3215.

464 Beyer, G. B., Costanzo, C., and Heinemann, D. (1996). Modifications of the  
465 Heliosat procedure for irradiance estimates from satellite images. *Solar*  
466 *Energy*, 56:207–212.

467 Bishop, C. M. (2006). *Pattern Recognition and Machine Learning (Informa-*  
468 *tion Science and Statistics)*. Springer-Verlag, Berlin, Heidelberg.

- Cazes-Boezio, G., Robertson, A. W., and Mechoso, C. R. (2003). Seasonal dependence of ENSO teleconnections over South America and relationships with precipitation in Uruguay. *Journal of climate*, 16(8):1159–1176.
- Ceballos, J. C., Bottino, M., and de Souza, J. (2004). A simplified physical model for assessing solar radiation over Brazil using GOES 8 visible imagery. *Journal of Geophysical Research: Atmospheres*, 109(D2).
- Cebecauer, T., Šúri, M., and Perez, R. (2010). High performance MSG satellite model for operational solar energy applications. In *Proceedings of the American Solar Energy Society (ASES)*, pages 1–5, Phoenix, Arizona, United States.
- Diabate, L., Blanc, P., and Wald, L. (2004). Solar radiation climate in africa. *Solar Energy*, 76.
- Duda, R. O., Hart, P. E., and Stork, D. G. (2001). *Pattern Classification*. Wiley, New York, 2 edition.
- Grimm, A. M., Barras, V. R., and Doyle, M. E. (2000). Climate variability in southern South America associated with El Niño and La Niña events. *Journal of Climate*, 13:35–58.
- Iqbal, M. (1983). *An introduction to solar radiation*. Academic Press.
- Jolliffe, I. T. (2002). *Principal Component Analysis, Second Edition*. Springer.
- Justus, C. and Paris, M. V. (1986). Satellite-measured insolation in the

- 490 united states, mexico, and south america. *Remote Sensing of Environment*,  
491 20:57–83.
- 492 Laguarda, A., Giacosa, G., Alonso-Suárez, R., and Abal, G. (2020). Per-  
493 formance of the site-adapted CAMS database and locally adjusted cloud  
494 index models for estimating global solar horizontal irradiation over the  
495 Pampa Húmeda. *Solar Energy*, 199:295–307.
- 496 Maciel, F., Terra, R., and Chaer, R. (2015). Economic impact of considering  
497 el Niño-Southern Oscillation on the representation of stream flow in an elec-  
498 tric system simulator. *International Journal of Climatology*, 35(14):4094–  
499 4102.
- 500 Mechoso, C. R. and Pérez-Iribarren, G. (1992). Streamflow in southeastern  
501 South America and the Southern Oscillation. *Journal of Climate*, 5:1535–  
502 1539.
- 503 Noia, M., Ratto, C., and Festa, R. (1993a). Solar irradiance estimation from  
504 geostationary satellite data: I. statistical models. *Solar Energy*, 51(6):449  
505 – 456.
- 506 Noia, M., Ratto, C., and Festa, R. (1993b). Solar irradiance estimation from  
507 geostationary satellite data: II. physical models. *Solar Energy*, 51(6):457  
508 – 465.
- 509 Perez, R., Ineichen, P., Moore, K., Kmiecik, M., Chain, C., George, R.,  
510 F., and Vignola (2002). A new operational model for satellite-derived  
511 irradiances: description and validation. *Solar Energy*, 73:307–317.

- Pisciottano, G., Díaz, A., Cazes, G., and C.R., M. (1994). El Niño-Southern 512  
Oscillation impact on rainfall in Uruguay. *Journal of Climate*, 7:1286 – 513  
1302. 514
- Polo, J., Gastón, M., Vindel, J., and Pagola, I. (2015). Spatial variability 515  
and clustering of global solar irradiation in vietnam from sunshine duration 516  
measurements. *Renewable and Sustainable Energy Reviews*, 42:1326–1334. 517
- Qu, Z., Oumbe, A., Blanc, P., Espinar, B., Gesell, G., Gschwind, B., Klüser, 518  
L., Lefèvre, M., Saboret, L., Schroedter-Homscheidt, M., and Wald, L. 519  
(2017). Fast radiative transfer parameterisation for assessing the sur- 520  
face solar irradiance: The Heliosat-4 method. *Meteorologische Zeitschrift*, 521  
26(1):33–57. 522
- Rigollier, C., Lefevre, M., and Wald, L. (2004). The method Heliosat-2 for 523  
deriving shortwave solar radiation from satellite images. *Solar Energy*, 524  
77(2):159–169. 525
- Tarpley, J. (1979). Estimating incident solar radiation at the surface from 526  
geostationary satellite data. *Journal of Applied Meteorology*, 18(9):1172– 527  
1181. 528
- Trenberth, K. E. (1997). The definition of El Niño. *Bulletin of the American* 529  
*Meteorological Society*, 78(12):2771–2778. 530
- Watanabe, T., Takamatsu, T., and Nakajima, T. Y. (2016). Evaluation of 531  
variation in surface solar irradiance and clustering of observation stations 532  
in japan. *Journal of Applied Meteorology and Climatology*, 55(10):2165– 533  
2180. 534

- 535 Wilks, D. (2011). *Statistical Methods in the Atmospheric Sciences, 3rd edi-*  
536 *tion*. International geophysics series (v100). Academic Press.
- 537 Zagouras, A., Inman, R., and Coimbra, C. (2014). On the determination  
538 of coherent solar microclimates for utility planning and operations. *Solar*  
539 *Energy*, 102:173–188.
- 540 Zagouras, A., Kazantzidis, A., Nikitidou, E., and Argiriou, A. (2013). Deter-  
541 mination of measuring sites for solar irradiance, based on cluster analysis  
542 of satellite-derived cloud estimations. *Solar Energy*, 97:1–11.
- 543 Zagouras, A., Kolovos, A., and Coimbra, C. (2015). Objective framework for  
544 optimal distribution of solar irradiance monitoring networks. *Renewable*  
545 *Energy*, 80:153–165.